RICE UNIVERSITY

Segmentation and Visualization of Volume Maps

by

Powei Feng

A Thesis Submitted
in Partial Fulfillment of the
Requirements for the Degree

Master of Science

Approved, Thesis Committee:

[illegible]

Joe Warren, Professor, Chair
Computer Science

[illegible]

Ron Goldman, Professor
Computer Science

[illegible]

Luay Nakhleh, Assistant Professor
Computer Science

Houston, Texas

April, 2010

Segmentation and Visualization of Volume Maps

Powei Feng

Abstract

Volume data is a simple and often-used representation for exchanging and processing data in various scientific domains, such as medicine and molecular biology. The segmentation of volume data is an essential part of data interpretation. Researchers have extensively studied the problem of segmentation focusing on efficient algorithms for segmenting and rendering volumes. Our contribution is two-fold. First, we propose a tri-linear classification method that can implemented on the GPU to reduce artifacts and jaggedness along the material boundaries that appear when rendering segmented volumes. Our representation provides sub-voxel accuracy for representing segmented materials. Second, we demonstrate our interactive painting-based segmentation tool, which can be used to rapidly produce an intuitive segmentation. We compare our tool against known results and show that we can generate similar segmentations using a simple and intuitive control scheme.

Acknowledgements

I would like to thank Joe Warren, my advisor, not only for introducing the problem to me but also for providing careful guidance throughout this research. I would also like to thank Ron Goldman for detailed comments on how to improve this thesis. I also thank Luay Nakhleh for serving as part of my committee and imparting helpful suggestions during the defense.

Contents

Illustrations

Chapter 1

Introduction

Volume data is defined by a three-dimensional grid of scalar values or tuples. Each point on the grid is called a *voxel.* (The two-dimensional version of volume data is a grey-scale or colored image). Volume data can be generated for simulations or generated through imaging technology such as computed tomography (CT) in medicine and electron microscopy (EM) in bio-molecular imaging. The most intuitive analysis of a 3D volume map is through visualizing the data. For example, given a CT scan of a hand, we can reconstruct a 3D model of the hand that allows for interactive visual manipulation such as rotation, translation, and magnification. In addition to visualizing the entire volume, sometimes it is useful to visualize the components that reside within a volume map. (In the case of the hand CT, it would be useful if we can separate out the bones from the flesh). To visualize components within a volume, the first step is to separate out regions of interest within the data set. This separation is called *segmentation.* Besides bone/flesh separation in medicine, segmentation also corresponds to other high-level semantics such as locating symmetric subunits from a reconstructed image of a protein (see Figure 1.5(b)) and identifying individual parts of a mechanical object like an engine (see Figure 1.5(d)).

Our work addresses the specific problem of visualizing segmented volumes. We focus on reducing the jagged boundary associated with binary classification of segmented volumes. In addition to visualization, we also develop a semi-automatic segmentation interface and demonstrate that this interface is an intuitive and efficient method for segmentation.

In the rest of this chapter, we will discuss the background and motivation of our work on volume visualization and segmentation. We will also briefly describe our approach, which is elaborated in the following chapters.

1.1 Visualizing Volume Data

Visualizing volume data requires interpreting the discretely-sampled volume as a continuous function. One approach is to interpret the space between samples as a tri-linear interpolation function by treating the discrete samples as the interpolant at the corners of the function domain. The entire domain of the volume is then covered by piece-wise tri-linear functions. To display the function defined on the volume, we can choose a threshold value and extract a level-set from the combined function. This approach is a form of implicit modeling, which is a standard technique for modeling shapes in computer graphics [1]. Given a function $f(x, y, z)$ (our previously defined volume function), the set of all points such that $f(x, y, z) < 0$ defines the one region and the set of all points such that $f(x, y, z,) > 0$ defines a second, complementary region (excluding the surface where the function is zero). For a multiple material viewpoint, the implicit function $f(x, y, z)$ partitions space into two materials; one material where the function $f(x, y, z)$ is positive and another where $f(x, y, z)$ is negative. Numerous contouring method such as Marching Cubes [15], Dual Contouring [9] and others [5, 12, 20] can then generate a polygonal surface that separates the positive space from negative space.

Alternatively, the two spaces can be visualized using various volumetric approaches implemented on the GPU [28, 4, 22]. The key ideas behind these approaches are that the signed grid can be stored as a 3D texture and that a single texture load can be used to evaluate $f(x, y, z)$ via tri-linear interpolation at an arbitrary point. In practice, this tri-linear boundary surface provides better normals for shading and better silhouettes than the discrete voxelized approach.

While the use of two signs to distinguish between two materials is simple and elegant, the idea of using three or more signs to represent a partition of space into

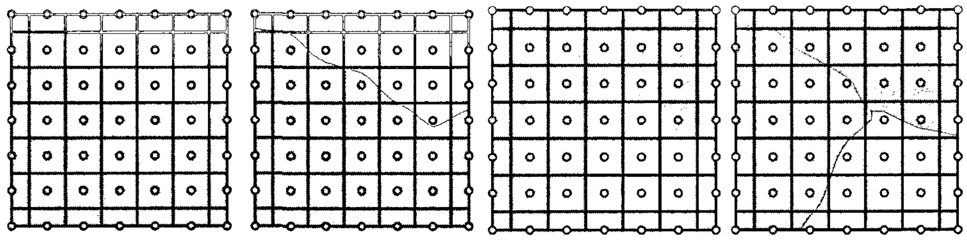

(a) Two material binary classification (b) Two material +/- bilinear contour (c) Three material binary classification (d) Three material bilinear contour

Figure 1.1 : 2D example of segmented volume visualization. 1.1(a) shows the input segmented volume, and 1.1(b) renders a piecewise bi-linear function over the segmented domain. Note that the bi-linear classification produces smoother boundary but also maintains the correct partition. 1.1(c) and 1.1(d) are the three material variants.

multiple material has received only limited attention. A simple representation of a segmented volume map is to attach an auxiliary discrete volumetric grid whose voxels each consist of a single material, which can be denoted with integers. The materials comprising the volumetric grid can be stored as a 3D array of integers. While this approach is fairly simple to implement, its drawbacks are obvious. The resulting materials have blocky boundaries that are hard to shade in a natural manner and have jagged silhouettes and inter-material boundaries [7] (see Figures 1.1(c) and 1.2(c)).

In Ju et al's Dual Contouring, in which material indices are attached to a grid to represent three or more materials [9]. In this approach, the boundaries between materials are represented as polygonal surfaces created from point and normal data stored on edges in the grid. Ju et al's work assumes that auxiliary data (such as edge intersections) is provided in addition to the volume. In our work, we make no assumption about the data beyond the segmentation of the volume. Other researchers have studied multiple material rendering in different contexts. Fujimori et al. and Shammaa et al. focus on the related problem of extracting multi-material surfaces from volume maps that do not have labeled voxels [6, 25]. Their extraction involves

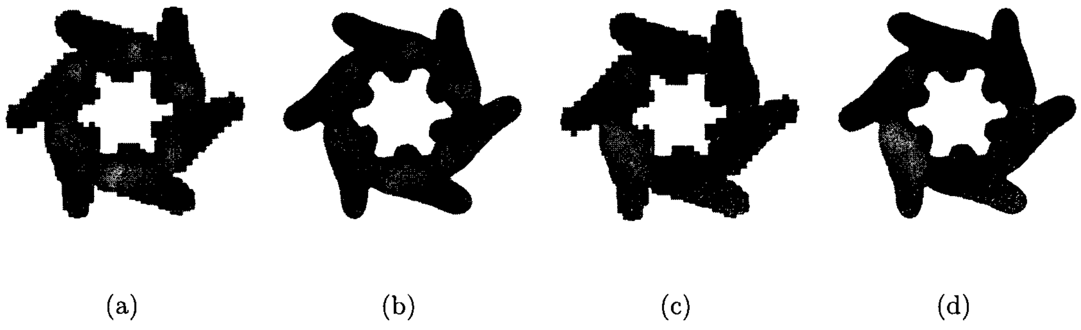

Figure 1.2 : Example of segmentation and our multi-material representation. 1.2(a) illustrates a typical segmented material over a low-resolution map. The segmentation is performed by thresholding. 1.2(b) shows the same material under our representation. 1.2(c) shows the same map after further segmentation. 1.2(d) shows our representation after the second segmentation. This example is the replicative helicase G40P molecular structure.

surface construction with respect to inter-material threshold values. In contrast, our work assumes that segmentation is defined by voxel labeling.

Researchers have also tried to alleviate the voxelization defects of discrete classification for segmented volumes. Kadosh et al. and Gibson both describe interpolation methods for smoothing out binary density maps by using scalar maps that represent distances to the surface [10, 7]. In comparison, our scalar map generalizes to three or more materials, and our representation enables a texture-based GPU implementation for rendering. Stalling et al. presents a scheme for sub-voxel contours by attaching probabilities to each voxel and bilinear interpolating for arbitration between materials [26]. Though our approaches are similar, our work describes a more compact representation of the scalar field that extends from the two-material case. We also show how our representation can be efficiently implemented in the GPU.

In another significant work on multi-material rendering, Tiede et al. introduced a multi-material classification scheme for volume raycasting [27]. Hadwiger et al. integrated this classification scheme into their hardware implementation of high-quality

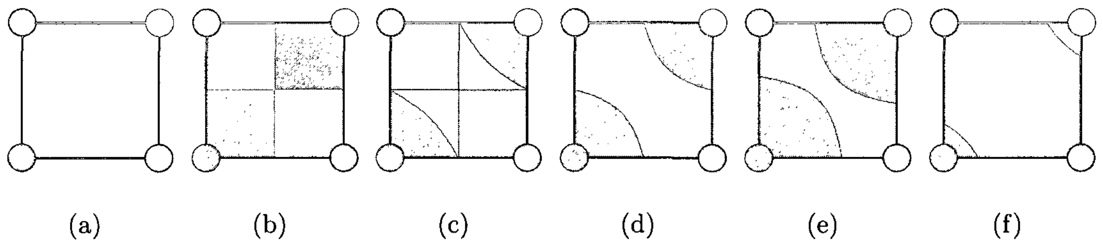

Figure 1.3 : Two-dimensional comparison of methods. (a) is a multi-material voxel with no intensity information. (b) is the naive approach of classifying by nearest neighbor. (c) Tiede et al. proposes a linear filter for classification [27], but it leaves points unclassified. (d) We propose a tri-linear representation that classifies all points within a voxel. (e) and (f) are examples of our approach that demonstrate the flexibility in representing contours.

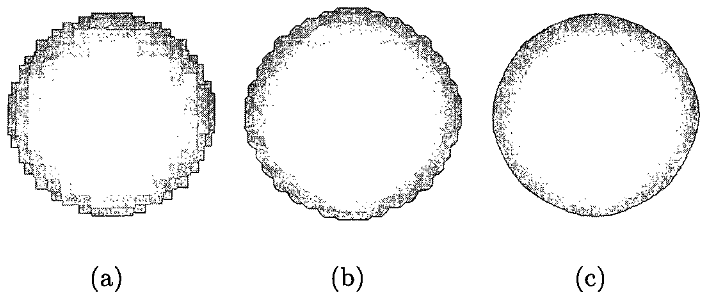

Figure 1.4 : Three-dimensional comparison of methods. (a) is the input of a sphere-like segment. (b) is rendered using Tiede et al.'s classification scheme [27]. Note that it produces a bumpy surface. (c) is our representation for the segment contour. Details for constructing (c) from the segment (a) is described in Section 3.4.

volume rendering [8]. The classification scheme described by Tiede et al. focuses on segments produced by thresholding. In the case where the threshold ranges of multiple materials overlap, Tiede et al.'s approach is to linearly interpolate the binary mask associated with the material. For each material A, space where the interpolated value (with respect to A's tri-linearly interpolated binary mask) is greater than 0.5 is classified as A. Although linear filtering resolves the overlap of threshold ranges, it also produces unclassified regions within a single voxel (see Figure 1.3(c)). In the case where the input is a segmented volume without intensity information, Tiede et al's approach would produce a classification that has ripple-like effect (see Figure 1.4(b)). Our method guarantees classification for all points within a voxel (see Figure 1.3(d)) and provides greater flexibility in sub-voxel classification (see Figure 1.3(e)), hence capable of representing smooth inter-material boundary (see Figure 1.4(c)) . Also note that both Tiede et al. and Hadwiger et al. tackled the problem from a visualization perspective, where they improved multi-material rendering for one particular visualization technique. Our approach is to present a geometric representation for multi-material volume that can be used for various visualization methods.

Our approach is to generalize the idea of two-sign tri-linear contouring to that of multi-sign tri-linear contouring with the goal of creating a partition of space into disjoint materials whose boundaries are piecewise tri-linear surfaces. The advantage of this approach is that the resulting material boundaries would better approximate given boundaries and reduce rendering artifacts inherent in voxel rendering. Our fundamental approach to multi-material contouring is viable for any type of implicit function and not restricted to the tri-linear case. Figure 1.5 shows how our approach reduces the artifacts of the input segmented volume.

1.2 Volume Segmentation

In conjunction with our contribution on visualization, we also present a simple method for rapid segmentation. Segmentation is the process of partitioning a set voxels into subsets, each of which is called a segment. More formally, segmentation can be viewed as the partition of voxels coordinates. Let V be the input volume. V defines a function in 3-Space where $V : \mathbb{N}^3 \longrightarrow Y$ and Y can be a space of any finite dimension (usually $Y = \mathbb{R}$). The volume data is discrete so there exists a finite set $X \subsetneq \mathbb{N}^3$ such that a point p is in X if and only if $V(p)$ is well-defined. Finally, segmentation is the construction of sets $S_1, S_2, \ldots, S_n$ where $S_i \subseteq X$, and each of the S_i is called a segment. Two other common requirements are that $\cup_{i=1 \ldots n} S_i = X$ and $S_i \cap S_j = \emptyset$ for $i \neq j$. These two conditions express the disjoint-union property for segmentation.

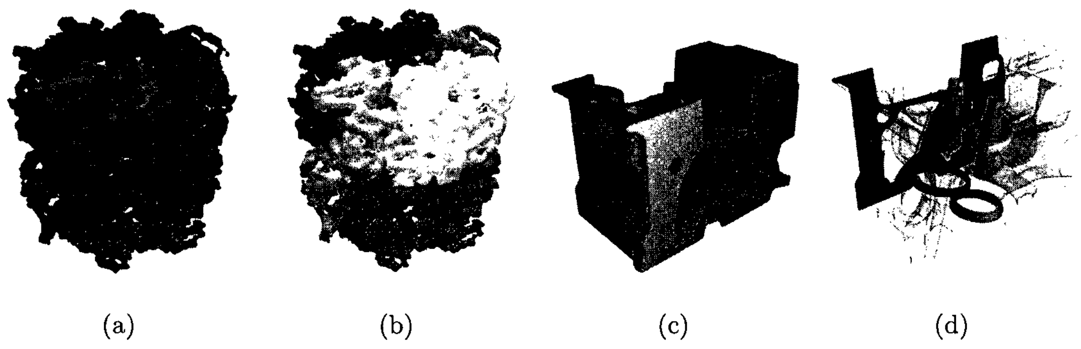

Figure 1.5 : The GroEL molecular structure and an engine block. 1.5(a) shows the raw density map, and 1.5(b) is the result of its segmentation into 14 subunits using our tool. 1.5(c) shows the raw engine data and 1.5(d) shows the result of the segmentation with transparency.

Figure 1.5 shows raw volumes before and after segmentation.

Many researchers have studied the problem of 3D segmentation in different domains. In particular, automatic methods for segmenting volume data have received much attention. Automatic techniques usually involve quantifying low-level features to identify regions of interest in each specific data set. Such features include similarity in values between voxels, proximity of voxels, and values of high-order derivatives of the implicit function. Various techniques have been explored on this front including thresholding, region growing, and water-shed [29]. However, automatic methods suffer from an excess of parameter manipulation. The user often has to repeat the process of inputting parameters and executing the algorithm to perform segmentation. Moreover, each automatic segmentation technique is tailored towards a specific problem. Transferring a technique across problem domains often results in poor segmentations because segmentations often require semantic interpretations and different domains have different semantics attach to their segmentation. Emulating human semantics in one domain is already a difficult task, and trying to emulate all the possible semantics that could arise in all domains is a far more daunting problem.

In contrast to a fully automatic approach, other works focus on semi-automatic methods that require some level of user input. These methods provide more accuracy and more control over automatic methods. Work in this area involves using an input device (i.e. the mouse) and marking the segments manually. Given enough user input, automatic techniques can then be applied to the volume with greater accuracy. The additional input from the user helps guide the automatic process, and using automation prevents the user from manually marking the entire volume, which can be an error-prone and time consuming process.

Previous works on semi-automatic methods include Owada et al.'s Volume Catcher and Yuan et al.'s Volume Cutout [19, 29]. Volume Catcher allows the user to draw 2D free-form strokes on volume; the strokes are then extended using region growing and set as constraints for graph-based segmentation. Volume Cutout uses two kinds of strokes to denote the foreground and the background on a two-dimensional view of the 3D volume. The strokes are then used in a graph-based approach to automate the segmentation for the rest of the volume. These two approaches both focus on the problem of two-material segmentation. We are interested in generalized, multi-material segmentation.

Another difficulty in semi-automatic segmentation is in manipulating 3D objects using a 2D interface. Many of the existing methods involve extending 2D segmentation techniques by applying segmentation to 2D slices and re-constructing the 3D segmentation. However, it is hard to identify 3D spatial correlation and features using this approach. We choose an approach that operates directly on the 3D volume with semi-automated segmentation using graph-cut. Graph-cut methods have proven to be useful for segmenting 2D images. Typically, 2D graph-cuts involve denoting the foreground and background of the graph/image through user input and performing a min-cut/max-flow variant to identify two sets of nodes/pixels. The min-cut induces a natural component partition across the image that satisfies the criterion of segmentation. The 3D complement of this approach has been used by Liu et al. for bone segmentation [14]. Their work takes the rectilinear grid as the graph for the cut. Seeds are placed by the user on 2D slices to perform segmentation. We build upon their method, using a 3D interface and complementing the process with hardware rendering that allows for interactive visualization and editing of volume data sets. Our tool lets the user partially paint the desired segmentation and fill in the unpainted portions by applying the graph-cut optimization.

The following chapters will be organized as the following: Chapter 2 will present the details of our visualization representation for segmented volumes; Chapter 3 will cover how our representation can be applied in practical settings; Chapter 4 will discuss our painting-based segmentation interface and present the results.

Chapter 2

Tri-linear Representation of Segmented Volumes

2.1 Multi-material Contouring

2.1.1 Classification method

Our approach for multi-material contouring is to replace a signed grid of scalars with a grid whose vertices have an associated scalar and material. In the two material case, our method should reproduce the standard $+/-$ interpretation using normal contouring. In the case of three or more materials, the contouring method should generate piecewise tri-linear contours that join continuously along the faces of the grid.

Given a grid cell whose corners have associated non-negative scalars s_i and material indices m_i, the following method can be used to determine the material index of a point x inside the cell. The index i ranges from 0 to 7, representing the eight corners of a cell.

Material Classification Method

- For each distinct material index present in the cell, construct a set of scalars t^k associated with the corners of the cell via the following rule:

$$\begin{aligned} t_i^k &= s_i \quad \text{if } k = m_i \\ t_i^k &= 0 \quad\;\; \text{otherwise} \end{aligned}$$

- Compute the values of the tri-linear interpolant $t^k(x)$ for each distinct index k. The tri-linear coefficients are t_i^k for $i = 0, 1, \ldots 7$.

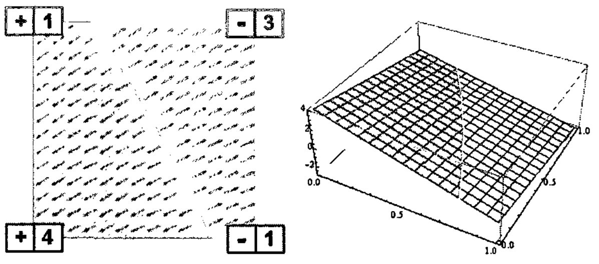

Figure 2.1 : Two material example. 2.1(a) shows the bilinear function of a single cell. Red represents the parts of the cell that has positive values in the bilinear evaluation, and green represents the negative values. The arrows indicate the direction of the gradient. 2.1(b) is the plot of the bilinear function in 3D with the same color representation.

- Return the material index k for which $t^k(x)$ is maximum.

This classification method has several important properties. The first property is that the classification method reproduces the contours produced by standard $+/-$ contouring. Given a signed set of scalars s_i, the associated tri-linear interpolant $s(x)$ is either positive or negative. According to our material classification method, the coefficients s_i can be partitioned in a two sets of non-negative coefficients t_i^+ and t_i^-. Note that these coefficient sets satisfy the relation

$$s_i = t_i^+ - t_i^- \tag{2.1}$$

Therefore, the associated tri-linear functions $t^+(x)$ and $t^-(x)$ also satisfy

$$s(x) = t^+(x) - t^-(x). \tag{2.2}$$

It follows that the function $s(x)$ is positive if $t^+(x)$ is larger than $t^-(x)$ and negative if $t^-(x)$ is larger than $t^+(x)$, agreeing with the result computed by our classification algorithm.

Figure 2.1 illustrates the standard bi-linear approach to contouring in 2D. Figure 2.1(a) shows a single cell whose corners have attached signed scalar values. Fig-

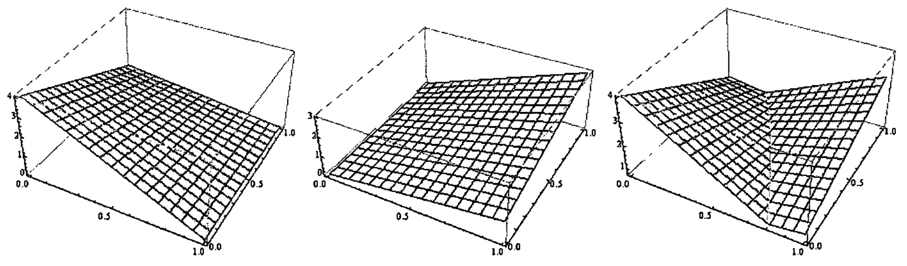

Figure 2.2 : 2 material example continued. 2.2(a) is the plot of the function in 2.1 by replacing the negative voxels (coefficients of the bilinear) with 0's. 2.2(b) is the plot of the same function by replacing the positive voxels with 0's and taking the absolute value of the coefficients. 2.2(c) is the maximum of the functions in 2.2(a) and 2.2(b).

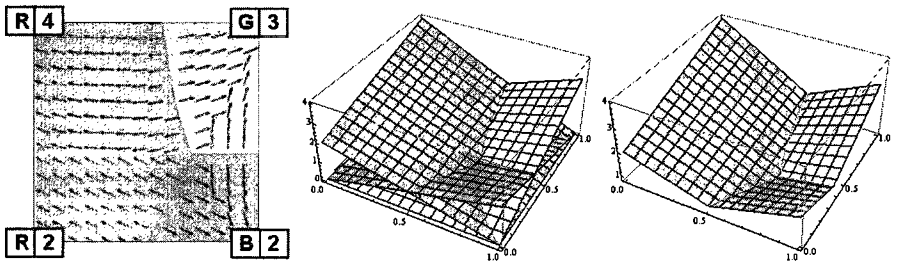

Figure 2.3 : 3 material example. 2.3(a) is the classification of the bi-linear function under our scheme. The arrows denote the gradient. 2.3(b) is the plot of 3 functions that are created under our evaluation scheme. 2.3(c) is the maximum plot of the three functions.

ure 2.1(b) shows the associated bi-linear $s(x)$ interpolant partition into positive and negative regions. Figure 2.2 illustrates our classification method on this example. Figures 2.2(a) and 2.2(b) shows the functions $t^+(x)$ and $t^-(x)$, respectively. Figure 2.2(c) shows a plot of the maximum of these two functions. Note that the partition of the pixel in figures 2.1(b) and 2.2(c) are equivalent.

Figure 2.3(a) shows another 2D example in which the four corners of the pixel have three distinct materials, red, green and blue. Figure 2.3(b) show plots of the three bi-linear functions associated with the materials. Finally, Figure 2.3(c) shows a plot of the maximum of these functions and the associated partition of the pixels into three distinct materials via three bi-linear contours that meet at a common point.

2.1.2 Characterization of the Contours

The multi-material contours produced by this method have several important properties. First, the contours are continuous across cells sharing a common face. This fact follows from the observation that two cells sharing a common face have the same scalars and material indices on that face. Since the restriction of the tri-linear functions used in defining the multi-material contour on this face depend only on the scalar and material indices on that face, the multi-material contours must agree.

Piecewise Tri-linear Surfaces

Inside a single cell, the resulting contours are simply piecewise contours of various tri-linear functions. To understand why, note that the contours bounding the region associated with a material with index k are simply surfaces where the tri-linear function $t^k(x)$ and another tri-linear function $t^j(x)$ both reach the maximum. Therefore, this contour is an iso-surface of the form

$$t^k(x) = t^j(x)$$

We have used a GPU-based, volume rendering approach to find the contour in our implementation. However, it is possible to solve this classification problem using polygonal methods such as Dual Contouring. Under Dual Contouring, we find a point within the cell that best describes the intersection of all the pairwise tri-linear surfaces. More formally, let M be the set of materials within a cell and let x be a point inside the cell. Consider the function

$$E(x) = \sum_{j,k \in M, j \neq k} (t^k(x) - t^j(x))^2 \tag{2.3}$$

The minimum of this function describes a point that is closest to the intersection of all the surfaces that satisfy $t^k(x) = t^j(x)$. This is a non-linear optimization problem that can be costly to compute. We approximate the solution using an QEF-based approach that is described by Schaefer et al [24]. This method locates the intersections, p_i, of the surfaces along the cell edges. These intersections and the normals, n_i, at these points describe a set of planes per cell. We then find a point that minimizes

$$E'(x) = \sum_i (n_i \cdot (x - p_i))^2 \tag{2.4}$$

This minimization gives an approximation of Eq. 2.3 that is reasonable for our purpose. Note that this is an outline for computing the contour point. Please refer to the work of Schaefer et al. for more implementation details [24].

Since we are replacing the tri-linear function in each cell with linear approximations, the contour may not retain enough details of the original function. We can retrieve these details by subdividing the grid space into finer cells. The new mask indices are determined by the classification method described previously; the new scalar for the refined map must be computed per each material. In effect, this approach will expand the storage size for the scalar by a factor of n, where n is the number of materials. This can be done adaptively to subdivide cells only along material border to reduce the computation and storage size. In our experiments, we perform a uniform subdivision over the entire volume, but we also notice that refinement is not necessary in most cases. Figure 2.4 shows the results of meshing using Dual Contouring.

Gradient

One useful property from standard implicit modeling is that the gradient of the implicit function is normal to the contours of that function. In the multi-material case, a similar property holds. Given a contour formed by the iso-surface $t^k(x) = t^j(x)$, the gradient of the function $t^k(x) - t^j(x)$ is simply the normal to this surface. The key observation here is that the pair of material indices j and k change as the point x varies

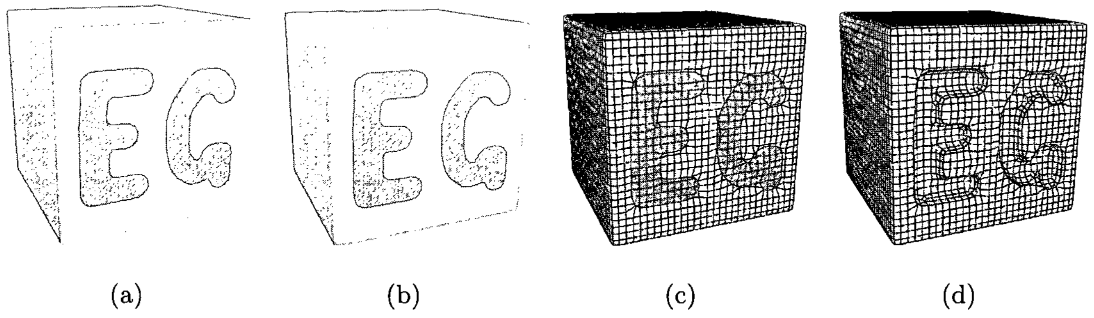

Figure 2.4 : The perspective view of a multi-material volume of size 33^3 rendered using GPU tri-linear contouring (a) and as polygonal contours generated by Dual Contouring (b), showing the grid structure (c). (d) depicts the mesh generated from Dual Contouring without the letters.

over the cell. For the three material case, $t^k(x)$ and $t^j(x)$ denote the largest and second largest tri-linear interpolant at x. Using the difference of the top two interpolated values will produce the exact gradient field, since we can view the local neighborhood of a point on the two-material boundary as defined by the two dominant tri-linear functions. Note that points where more than two materials meet are degenerate with unknown gradients. Figure 2.1(a) show the gradient field for a two material pixel, while Figure 2.3(a) shows the gradient field for a three material pixel.

2.2 Set Operations on Multi-material Contours

Given that the goal of this thesis is to apply multi-material contours to the problem of representing segmentations, we next develop analogs of the set operations Union and Intersection for multi-material contours. These operations will provide the basis for the painting operations described in the next section.

2.2.1 Operations on Two Materials

One of the primary attractions of implicit modeling is the ease with which it can model Boolean operations from constructive solid geometry [23, 18]. In the signed (two-material) case, the typical convention is to represent a solid as the set of solutions to the inequality $f(x, y, z) < 0$. Now, given two solids $f(x, y, z) < 0$ and $g(x, y, z) < 0$, the union of these two solids is simply the set $\min(f(x, y, z), g(x, y, z)) < 0$ while the intersection of two solids is the set $\max(f(x, y, z), g(x, y, z)) < 0$.

If the functions f and g are represented by signed grids, a standard technique for approximating their union or intersection is to take the min or max of their associated sign grids. Our goal is to develop equivalent rules for the two-material case that generalize to the multi-material case in a natural manner.

Our approach is as follows; consider two materials A and $\neg A$ (not A). A can be interpreted as being the inside of a solid (i.e; negative in the implicit model) and $\neg A$ can be interpreted as being the outside of a solid (i.e; positive in the implicit model.). Given a multi-material map consist of only these two materials, we can attempt to construct rules for computing new non-negative scalars and material indices on the grid that reproduce the operations Union and Intersection.

In particular, give a grid point with two associated pairs (s_1, k_1) and (s_2, k_2) (where both the s_i are non-negative), our goal is to compute a scalar/index pair (s, k) for the union of the material S. This new pair can be computed using the following case look-up given in Table 2.1.

Note that the rule for computing k is straightforward. For Union, the new material index is A if and only if at least one of the material indices is A. For Intersection, the new material index is A if and only if both of the material indices are A. The rule for computing the new scalar s is only slightly more involved. The key is converted back to the signed case and then return the result of taking the min of the converted scalars. For example, if both material indices are A, we take the negative of both scalars s_1 and s_2, compute their min and then negate the result. These three operations are simply the equivalent of taking the max of the original scalars. In particular, if both s_1 and s_2 are non-negative,

$$\max(s_1, s_2) = -\min(-s_1, -s_2) \qquad (2.5)$$

Union				Intersection			
k_1	k_2	k	s	k_1	k_2	k	s
A	A	A	$\max(s_1, s_2)$	A	A	A	$\min(s_1, s_2)$
A	$\neg A$	A	s_1	A	$\neg A$	$\neg A$	s_2
$\neg A$	A	A	s_2	$\neg A$	A	$\neg A$	s_1
$\neg A$	$\neg A$	$\neg A$	$\min(s_1, s_2)$	$\neg A$	$\neg A$	$\neg A$	$\max(s_1, s_2)$

Table 2.1 : Rules for performing Intersection and Union operations. We consider the pairs (s_1, k_1) and s_2, k_2, as the input. The output of Union and Intersection is denoted as pair (s, k).

Similar argument can be used to derive the formulas given for the remaining cases. Another interpretation of these operations on the scalars s_1 and s_2 is to view these numbers as estimate of the distance from the grid point to the boundary of the region A. In the case of Union, the rule is that if both grid points lie in A, a good estimate of the distance from the grid point to the boundary of the union is the maximum of these two distances. Similar arguments again apply in the other cases.

2.2.2 Operations for Three or More Materials

Given the method for union and intersection defined above, the generalization of these operations to three or more materials is relatively easy. We suggest two operations analogous to Union and Intersection for the multi-material case. The first operation Overwrite takes a multi-material map and a two-material map (with material A and $\neg A$) and performs the multi-material analog of Union. In particular, it treats the material in the first multi-material map as either A or $\neg A$ and applies the two material rules for Union described above. The result of an Overwrite operation is that the material A in the second map overwritten onto any existing materials in the first map. The resulting map contains the union of the materials A in both maps.

model	size	basic (fps)	classify (fps)
engine	$256 \times 256 \times 256$	34	14
foot	$256 \times 256 \times 256$	37	10
head	$128 \times 256 \times 256$	40	13
GroEL	$240 \times 240 \times 240$	38	16

Table 2.2 : The rendering speed for each of the data sets. All results were measured in Frames per Second (fps).

The second operation Restrict again takes as input a multi-material map and a two-material map (with materials A and $\neg A$). In this case, the Restrict operation modifies the second map to return the intersection of the first map (viewed as materials A and $\neg A$) and the second map. Essentially, the second map is restricted to only those regions where the material A exists in the first map.

2.3 Results

Our method has been implemented and tested on a Intel Xeon 5150 machine with 2 duo-core CPUs running at 2.66GHz. We use an nVidia GTX280 graphics card with 1GB of video RAM. The shaders are written in GLSL. We use OpenMP to enable multi-core processing for easily parallelizable portions of the code.

We gather rendering times for each of our test cases. The models are displayed in Figure 4.2. The running time largely depends on the maximum dimension of the volume as we use that to determine the number of quads to use as proxies for rendering. The rendering screen is 512×512 pixels. The intensive portion of the shader is called only for inhomogeneous cells, which implies that the rendering is slower for examples with a higher number of materials. This slowdown is evident in the "foot" example, where the number of materials is high. Note that the rendering speed also depends on the pixel estate required to display each volume; the smaller the volume appears on the screen, regardless of input size, the faster the rendering will be, which is as expected. Our results are taken from the slowest rendering time for each of the test sets. Our method maintains a reasonable frame-rate even under classification.

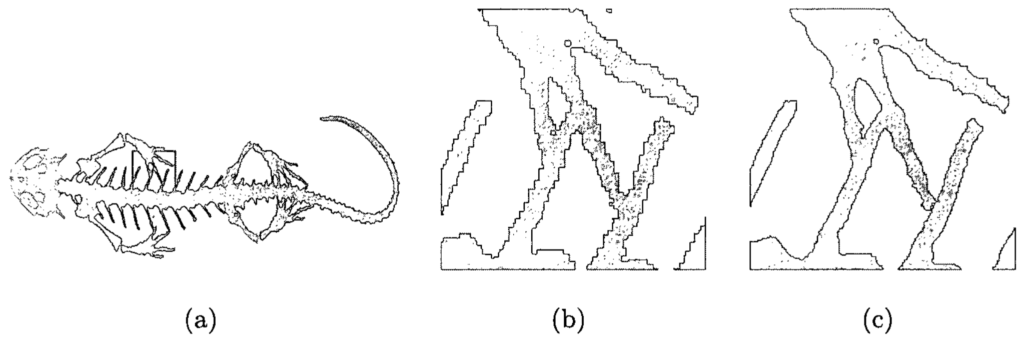

Figure 2.5 : A close up example of rendering using our piecewise tri-linear representation.

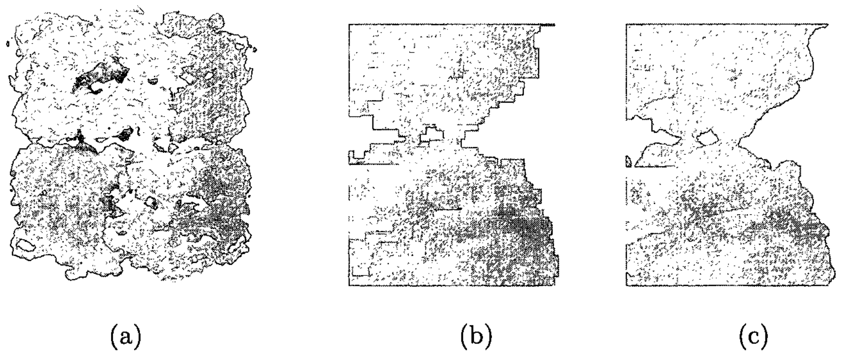

Figure 2.6 : A close up example of rendering using our piecewise tri-linear representation.

Chapter 3

Applications using Tri-linear Contours

3.1 Building Scalars from Existing Segmentation

In the case where segmented data are given as input, we present a simple heuristic to produce scalars off of the binary classification of a typical segmentation. Segmentation inputs are typically defined by associating an integer value at each voxel or by creating multiple 0-1 mask volumes, where each one represents a segment. Either of the two representation can be easily converted to the other. Without loss of generality, we assume the input is n 0-1 (binary) masks, where each masks represents one of n total segments.

Under our contour representation, we can an assign arbitrary scalar to each voxel, and the resulting surface should be a smoother surface than a binary classification. Unfortunately, this type of assignment does not produce desirable rendering of the segmented map (see Figures 3.1(b) and 3.1(e)). Instead, we blur each of the binary masks using a truncated $3 \times 3 \times 3$ gaussian function as our kernel [7]. We can view the output of the blurring as n scalars defined for each voxel, but the final output we want is a single scalar defined for each voxel. Using the convention defined previously, we write the following as the final output scalar, $t^{\text{new}}(x)$, at the voxel x.

$$t^{\text{new}}(x) = t^k(x) - t^j(x) \tag{3.1}$$

where $t^k(x)$ and $t^j(x)$ are the largest and second largest of the n values computed from the blurring step.

This heuristic is guided by the same intuition given in the *gradient* discussion of Section 2.1.2. In the two-material case, the contour will correspond the blurring of a

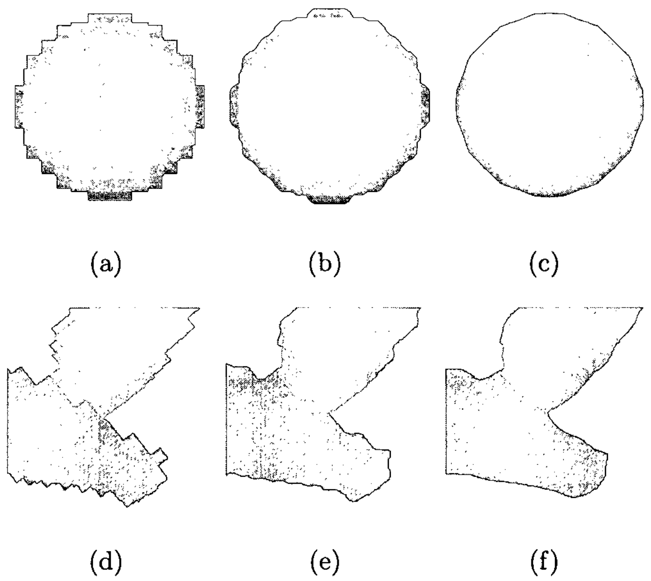

Figure 3.1 : These figures show the result of building scalars from existing segmentation. The top row of figures is a two-material example, and the bottom four figures represent the three-material case. 3.1(a) and 3.1(d) are the binary classification input. 3.1(b) and 3.1(e) are results of assigning all 1's as the scalar field. 3.1(c) and 3.1(f) are the results of blurring using the heuristic described in Section 3.1.

+/- density map. In the three material case, the contour is formed by the top two dominant trilinear interpolants ($t^k(x)$ and $t^j(x)$), and Eq. 3.1 is an approximation of that contour at the voxel x. Figure 3.1 shows the result of our heuristic. We see the improvement over the arbitrary assignment scheme.

3.2 Importing Iso-surfaces

One standard technique in volume visualization of a function $f(x, y, z)$ is to create a piecewise constant transfer function that highlights certain ranges of iso-values [13, 11]. Figure 3.2 shows an example of several nested iso-surfaces visualized in this manner.

This type of functionality can be reproduced in the multi-material setting in a natural manner. The basic idea is to import the various volumes bounded by the iso-

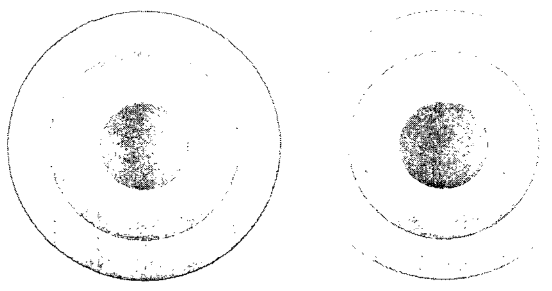

(a) (b)

Figure 3.2 : Figure 3.2(b) shows a multi-material map generated from the iso-surfaces of Figure 3.2(a).

surfaces as distinct materials using Overwrite and then assign some level of partial transparency to each material.

Given an iso-surface $f(x,y,z) = c$, we can construct a signed grid formed via samples of the function $f(x,y,z) - c$. Since the material boundaries are invariant up to multiplication by a scalar, we need to pick a normalization factor for the scalar field to ensure good utilization of the floating-point precision. First, we collect the voxel values along the contour c; for every cell that has densities above and below the contour level in its eight corner voxels, we store those values. We process the values so that a small percentage of the top and bottom values are discarded. This screens out extreme outliers that might force the majority of the values into a small range of the histogram. The maximum and the minimum of the truncated histogram are used to normalize the voxel values into the range $[0,1]$. These normalized values are used as part of the new scalar field S_{new}. Additionally, we store 1 in S_{new} for cells whose corner values are strictly above or below c. We then perform an Overwrite operation by overwriting S_{new} onto the old scalar field. The mask indices of grid values that are above c are set to a new mask value. This simple heuristic generates a single material that corresponds to a threshold segmentation.

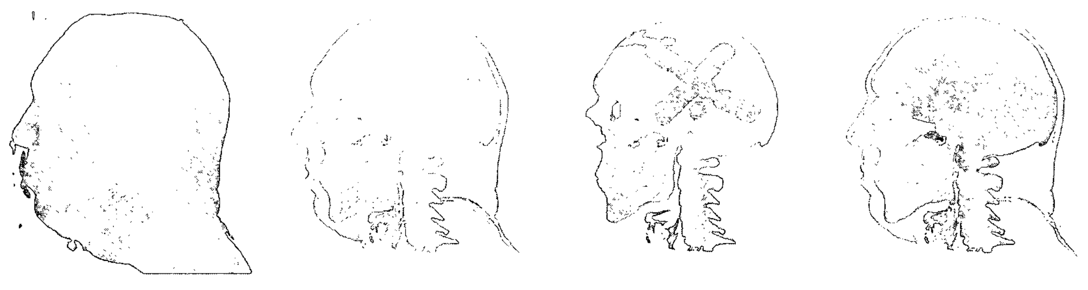

Figure 3.3 : Interactive painting-based segmentation of human head: the density volume 3.3(a), restricting painting to thresholded bones 3.3(b), user painting with spherical brush 3.3(c), and labeling result after graph-cut segmentation 3.3(d).

3.3 Tri-linear contours with Interactive Segmentation

We developed a simple painting-based segmentation interface to test and demonstrate our proposed representation. Our segmentation interface considers the input as a raw density map. The first step involves choosing one or more thresholds and generating material masks as described in Section 3.2. This step corresponds to an initial stage of segmentation by thresholding. Once these threshold materials have been generated, the user has the choice to turn the materials into visible or non-visible regions for painting. For example, when working on a human appendage, we can first turn the flesh invisible to paint and segment out the individual bones from the threshold level that corresponds to the bones. Figure 3.3 is an example of this process.

For painting, we provide the user with a spherical brush whose radius is variable. To position the sphere, we construct a ray that is perpendicular to the viewing plane and passes through the mouse position. The brush is positioned at the closest intersection point between the projecting ray the the visible regions.

The user can then hold down a button to indicate the start of a sweep. The sweep ends when the user releases the button. The sweep is constructed as a union of spheres, where the center of each sphere corresponds to the position of the mouse at some sampled instance during the the sweep. We compute a scalar field S_{sphere}, using the union of spheres and the computation detailed in Section 3.4. The S_{sphere} is then restricted to the visible region using the Restrict operation to build a new field S_{new}. The restriction will enable users to paint only on regions that are visible. After the restriction, we perform an Overwrite of the old scalar field with the new field S_{new}. All grid points that lie inside the union of spheres are assigned the mask index associated with the current brush.

Manual painting can be time-consuming. It is also prone to human error in controlling the painting device. Therefore, we decided to use automatic segmentation to aid our process. In particular, we find the graph-cut approach of segmentation to be very effective. We follow the method described by Liu et al. and extend it to a 3D interface [14]. We will briefly describe this method in the next chapter; please refer to Liu et al.'s work for more information. The scalars along the new inter-material boundaries can be computed using our method from Section 3.1 or the distance map method described by Gibson [7].

3.4 GPU-implementation

We use texture-based volume rendering as our algorithm for visualizing density maps. All volume maps (i.e. density map, auxiliary scalars, mask, etc.) are stored as 3D textures [28, 2]. Coloring a single screen fragment involves a number of texture loads to determine the density, color, and shade of the fragment in texture space. For our classification algorithm, we need to load an additional 8 scalar values and 8 integers as part of the fragment shader program. Texture loads are typically expensive operations in shader programming. However, these 16 loads can be reduced to 4 loads by packing the values into the RGBA channels for a single texel.

We store both the distance scalars and material masks as 8-bit textures, which allows up to 256 materials. With only 8-bits of precision for the distance scalars, we need to ensure that the precision is not wasted on non-essential portions of the representation. Note that the scalars are used for arbitration only on the border between different materials. This property implies that the scalars need to be accurate only for cells that intersect the inter-material boundary. We call a cell homogenous if its eight corners are marked as the same material; otherwise, a cell is inhomogeneous. For the spherical brush, we use the following distance metric for the new scalar field

$$\begin{aligned} g(x,y,z) &= |r - \sqrt{x^2+y^2+z^2}| \\ &\qquad \text{if } (x,y,z) \text{ is part of an inhomogeneous cell} \\ g(x,y,z) &= 1 \qquad\qquad \text{otherwise} \end{aligned} \tag{3.2}$$

Here r is the radius of the brush, and $x \in \{0, 1, \ldots, n_x - 1\}$ denote the grid space coordinates where n_x is the number of grid points in the x direction, and similar definitions holds for the variables y and z.

From Eq. 3.2 for any grid point (x, y, z) on a inhomogeneous cell, the associated scalar is bounded by $0 \leq g(x, y, z) \leq \sqrt{3}$. Because the Euclidean distance function ensures that the distance between any two points in a cell cannot exceed $\sqrt{3}$. In contrast, the squared distance function $\overline{g}(x,y,z) = |r^2 - (x^2 + y^2 + z^2)|$ does not have this property; that is, the absolute difference $|\overline{g}(p_1) - \overline{g}(p_2)|$ for any two points p_1, p_2 within a single cell is unbounded.

The bounded property of the Euclidean distance enables us to easily convert to an 8-bit representation, and it concentrates the precision only to inhomogeneous cells. This boundedness means that we can minimize the amount of texture memory and retain sufficient accuracy for our representation.

Chapter 4

Painting-based Segmentation

Painting assigns voxels into segments. Using our data representation, internally every voxel is associated with an integer, which we call the mask index or index. Visually, we use color to distinguish between two mask indices; that is, each mask index is assigned a color, and two different segments can be identified visually by their difference in colors.

Painting is performed in 3D using a spherical brush whose radius is adjustable. We determine the position of the brush by shooting a ray from the viewer eye position to the volume, where the direction of the ray is dictated by the mouse position. An intersection between the ray and the volume is computed by restricting the intersection to the first point on the ray with the visible volume. The point of intersection is used to place the center of the sphere. The user can then paint the volume by pressing a key, which indicates that all visible voxels within the sphere will be assigned a certain mask index. The visibility of a voxel is determined through the transfer function; a voxel v is visible if $T(f(v)) > \epsilon$ where T is the transfer function, f is the volume function, and ϵ is a small tolerance.

The mask indices are stored in a mask volume, which is updated per painting operation. We choose an index as the base index to represent the unpainted portion of the volume. Painting writes over the indices of the voxels contained within the sphere with the brush denoted index. To allow operations such as drilling through the volume, we also set the condition that the sphere will not intersect with a voxel that has the same index as the brush. This condition has the effect that the user can drill through the volume by repeatedly painting a region or gradually peel away the surface of a volume by painting only the outer surface. We also provide the option to hide or display a particluar segment. Hiding a segment can help the user to paint segments that might be occluded by other segments.

4.1 Segmentation with Graph-cut

The segmentation problem involves assigning each voxel a designation. Consider the graph induced by the inherent connectivity in the volume data. We let each voxel in the volume represent a node in the graph, and two nodes are connected if the manhattan distance between their corresponding voxels is 1. The problem is then viewed as a graph-cut problem: we want to find a minimum cut (a set of edges) that separates the graph into k connected components where two nodes are in different components if there does not exist a path that connects them with respect to the cut. This construction is a k-way min-cut/max-flow problem, which is known to be NP-Hard. However, the classical 2-way max-flow/min-cut problem is known to be solvable in polynomial time. Dahlhaus et al. proposes a simple approximation to the k-way min-cut problem by performing repeated 2-way cuts, taking the union of the cuts, and removing the cut with the largest sum of weights [3]. This method has a worst-case approximation ratio of 2.

Li et al uses the graph-cut approach in their segmentation, which is done through a 2D interface and seeding points. The users would select points on a 2D slice of the volume; each point denotes a point in the different segments. We build on their basic algorithm and extend it to a 3D interface. In our method, we let the user paint rough regions for each component of the segmentation; the user can then issue a command to grow each rough region automatically so that each region contains one approximate geometric component. Given n painted segments, we run n iterations of 2-way min-cut, where each iteration i is trying to grow segment S_i. We add the segmented voxels into the graph thus: for each iteration i, we consider the voxels marked as segment i as nodes that are connected to the source with infinite weight.

This iterative marking ensures that voxels chosen as part of S_i will not be re-colored as part of another segment. Furthermore, for all voxels v such that $v \in S_j$ where $j \neq i$, v is connected to the sink node with infinite weight. These edge connections ensure that segments that are already painted will not be over-written. All other visible voxels are considered to be free nodes in the graph. After a min-cut is performed, we classify all nodes in the graph as part of either the source or sink component of the graph. Voxels that correspond to nodes that are part of the source component will be re-grouped as part of S_i. This process is repeated for all S_i for $i = 1, \ldots, n$.

To reduce the size of the graph, we do not include colored voxels whose neighbors are all painted. These inner voxels do not affect the outcome of the cut as the edges that connect them cannot be removed under our construction of the graph. This constraint also implies that as the user paints more regions, the number of nodes in the graph-cut will reduce, and the min-cut will perform faster.

Note that our algorithm is not explicity finding an approximate minimum cut, but rather, heuristically separating the volume into components. Therefore, our cut does not maintain an approximation ratio of 2; furthermore, it is often the case that there will be un-colored voxels (or voxels that do not belong to a segment) at the end of the process. These regions will require further input from the user to be further segmented. Leaving voxels un-colored is an acceptable approach as the unpainted regions are often regions that require further input from the user.

4.2 Results

Our method has been implemented and tested on a Intel Xeon 5150 machine with 2 CPUs running at 2.66GHz. We use an nVidia GTX280 graphics card with 1GB of video RAM. The shaders are written in GLSL. We use OpenMP to enable multi-core processing for easily parallelizable portions of the code. We use the Boykov et al's implementation of min-cut, which has good practical running time.

model	volume size	nodes	segs	min-cut	total
engine	$256 \times 256 \times 256$	54485	7	8.89	123
foot	$256 \times 256 \times 256$	337546	19	27.22	157
head	$128 \times 256 \times 256$	368512	7	7.535	234
GroEL	$240 \times 240 \times 240$	589863	14	23.83	200
Hsp26	$128 \times 128 \times 128$	110875	13	3.05	95
pig	$512 \times 512 \times 134$	5109185	6	69.93	888
bunny	$512 \times 512 \times 361$	1825425	7	73.37	971

Table 4.1 : The timing results for segmenting various data sets. The "segs" column represents the number segments in the output. The "nodes" column represents the number of nodes in the induced graph. The min-cut column is the time (in seconds) to perform min-cut on the graph. The "total" column represents the total time (in seconds) to perform the segmentation.

4.2.1 Heterogenous Examples

Table 4.1 shows the approximate times it took to segment the different data sets. We chose 7 test sets of varying sizes and domains. We consider the user experience time in painting these data sets. Each model is painted three times with the best time being recorded. The painting time includes all processing time and the segmentation time. The processing time depends largely on the size of the segmentation graph and the number of segments. In our largest test case, the bunny, the induced graph has over one millon nodes and seven segments. The graph-cut algorithm for the bunny model runs on the order of a minute.

Except in the case of the two molecular structures, we do not have any expert knowledge on the proper segmentation; in most cases, we do not think there is an absolute baseline comparison. Therefore, we segment out components that we feel is an intuitive component of the whole. In the cases of molecular data, we have prior knowledge of the separation of the GroEL and Hsp26 structures into symmetric subunits.

The molecular data sets are the least difficult to segment. They have the property that corresponding graph connectivity between each symmetric subunit is low; this is exactly the optimal condition for the graph-cut to perform well. The two bone data share this characteristics as the connectivity between bone fragments is low. As indicated from Table 4.1, the time to segmenting each of the four data sets is less than five minutes. The piggy bank and bunny data sets presented the most difficulty in our tests. In all our tests, they were the largest in size. The time it took to perform single min-cut segmentation was on the order of a minute, and this hindered interactivity greatly. Furthermore, the piggy bank example was difficult due to the lack of distinct separation between the coins the the inner surface of the pig. Also problematic was the fact that the components were defined less by graph-connectivity and more by curvature. Both of these factors componded to slow the segmentation. The bunny example shared the connectivity/curvature problem, which contributed as well to its slower times. However, the two data sets were segmented in around fifteen minutes even with the aforementioned difficulties.

4.2.2 Protein Data Bank Examples

We have segmented datasets from the Protein Data Bank (PDB) entries. The PDB models are specified as a set of atomic coordinates, where each atom can have semantics attached to them. From the atomic coordinates, we build a volume over the dataset by convolving the atoms with a radial function, such as a gaussian [17]. For our purpose, we simply invoked the EMAN function `pdb2mrc` [16] to construct a volume over the input PDB. For comparison, we use a molecular visualization program called UCSF Chimera [21]. Chimera colors protein entries by chains. By examining the models visually, we reproduced the chain segmentation using our painting interface. Figure 4.1 illustrates that we were able to reproduce the segmentation closely.

Chapter 5

Conclusion

We present a technique for multi-material classification in the context of segmentation of density maps. Our classification method provides a smoother boundary than found in typical segmentation. Furthermore, it enables sub-voxel flexibility in shape-representation. This alleviates artifacts and jaggedness that can occur in visualization of segmented volumes.

We have also developed an intuitive segmentation interface that uses a graph-cut approach to combine user-knowledge and simplicity in segmentation. We have shown that our tool can be effectively used to rapidly create segmentation.

For our future work, we will experiment with using higher level interpolants such as B-splines for classification. This will give us greater flexibility and accuracy in defining the boundary between materials. Additionally, we will examine segmentation in the context of large cryo-electron tomography, which current techniques cannot address due to size and fidelity of the volume.

Bibliography

[1] Bloomenthal, J. Implicit surfaces. *Computer Aided Geometric Design 5* (1997), 341–355.

[2] Cullip, T. J., and Neumann, U. Accelerating volume reconstruction with 3d texture hardware. Tech. rep., Chapel Hill, NC, USA, 1994.

[3] Dahlhaus, E., Johnson, D. S., Papadimitriou, C. H., Seymour, P. D., and Yannakakis, M. The complexity of multiway cuts (extended abstract). In *STOC '92: Proceedings of the twenty-fourth annual ACM symposium on Theory of computing* (New York, NY, USA, 1992), ACM, pp. 241–251.

[4] Engel, K., Kraus, M., and Ertl, T. High-quality pre-integrated volume rendering using hardware-accelerated pixel shading. In *HWWS '01: Proceedings of the ACM SIGGRAPH/EUROGRAPHICS workshop on Graphics hardware* (New York, NY, USA, 2001), ACM, pp. 9–16.

[5] Frisken, S. F., Perry, R. N., Rockwood, A. P., and Jones, T. R. Adaptively sampled distance fields: a general representation of shape for computer graphics. In *SIGGRAPH '00: Proceedings of the 27th annual conference on Computer graphics and interactive techniques* (New York, NY, USA, 2000), ACM Press/Addison-Wesley Publishing Co., pp. 249–254.

[6] Fujimori, T., and Suzuki, H. Surface extraction from multi-material ct data. In *Computer Aided Design and Computer Graphics, 2005. Ninth International Conference on* (Dec. 2005), pp. 6 pp.–.

[7] GIBSON, S. F. F. Using distance maps for accurate surface representation in sampled volumes. *Volume Visualization and Graphics, IEEE Symposium on 0* (1998), 23–30.

[8] HADWIGER, M., BERGER, C., AND HAUSER, H. High-quality two-level volume rendering of segmented data sets on consumer graphics hardware. In *VIS '03: Proceedings of the 14th IEEE Visualization 2003 (VIS'03)* (Washington, DC, USA, 2003), IEEE Computer Society, p. 40.

[9] JU, T., LOSASSO, F., SCHAEFER, S., AND WARREN, J. Dual contouring of hermite data. In *SIGGRAPH '02: Proceedings of the 29th annual conference on Computer graphics and interactive techniques* (New York, NY, USA, 2002), ACM, pp. 339–346.

[10] KADOSH, A., COHEN-OR, D., AND YAGEL, R. Tricubic interpolation of discrete surfaces for binary volumes. *IEEE Transactions on Visualization and Computer Graphics 9*, 4 (2003), 580–586.

[11] KINDLMANN, G., AND DURKIN, J. W. Semi-automatic generation of transfer functions for direct volume rendering. In *VVS '98: Proceedings of the 1998 IEEE symposium on Volume visualization* (New York, NY, USA, 1998), ACM, pp. 79–86.

[12] KOBBELT, L. P., BOTSCH, M., SCHWANECKE, U., AND SEIDEL, H.-P. Feature sensitive surface extraction from volume data. In *SIGGRAPH '01: Proceedings of the 28th annual conference on Computer graphics and interactive techniques* (New York, NY, USA, 2001), ACM, pp. 57–66.

[13] LICHTENBELT, B., CRANE, R., AND NAQVI, S. *Introduction to volume rendering.* Prentice-Hall, Inc., Upper Saddle River, NJ, USA, 1998.

[14] LIU, L., RABER, D., NOPACHAI, D., COMMEAN, P., SINACORE, D., PRIOR, F., PLESS, R., AND JU, T. Interactive separation of segmented bones in ct

volumes using graph cut. In *MICCAI '08: Proceedings of the 11th international conference on Medical Image Computing and Computer-Assisted Intervention - Part I* (Berlin, Heidelberg, 2008), Springer-Verlag, pp. 296–304.

[15] LORENSEN, W. E., AND CLINE, H. E. Marching cubes: A high resolution 3d surface construction algorithm. In *SIGGRAPH '87: Proceedings of the 14th annual conference on Computer graphics and interactive techniques* (New York, NY, USA, 1987), ACM, pp. 163–169.

[16] LUDTKE, S. J., BALDWIN, P. R., AND CHIU, W. Eman: Semiautomated software for high-resolution single-particle reconstructions. *Journal of Structural Biology 128*, 1 (1999), 82 - 97.

[17] MURAKI, S. Volumetric shape description of range data using "blobby model". *SIGGRAPH Comput. Graph. 25*, 4 (1991), 227–235.

[18] OHTAKE, Y., BELYAEV, A., ALEXA, M., TURK, G., AND SEIDEL, H.-P. Multi-level partition of unity implicits. In *SIGGRAPH '05: ACM SIGGRAPH 2005 Courses* (New York, NY, USA, 2005), ACM, p. 173.

[19] OWADA, S., NIELSEN, F., AND IGARASHI, T. Volume catcher. In *I3D '05: Proceedings of the 2005 symposium on Interactive 3D graphics and games* (New York, NY, USA, 2005), ACM, pp. 111–116.

[20] PAIVA, A., LOPES, H., LEWINER, T., AND DE FIGUEIREDO, L. Robust adaptive meshes for implicit surfaces. In *Computer Graphics and Image Processing, 2006. SIBGRAPI '06. 19th Brazilian Symposium on* (Oct. 2006), pp. 205–212.

[21] PETTERSEN, E. Ucsf chimera-a visualization system for exploratory research and analysis. *J. Comput. Chem. 25* (2004), 1605–1612.

[22] REZK-SALAMA, C., ENGEL, K., BAUER, M., GREINER, G., AND ERTL, T. Interactive volume on standard pc graphics hardware using multi-textures

and multi-stage rasterization. In *HWWS '00: Proceedings of the ACM SIGGRAPH/EUROGRAPHICS workshop on Graphics hardware* (New York, NY, USA, 2000), ACM, pp. 109–118.

[23] Ricci, A. A Constructive Geometry for Computer Graphics. *The Computer Journal 16*, 2 (may 1973), 157–160.

[24] Schaefer, S., and Warren, J. Dual contouring: "the secret sauce". Rice University, Department of Computer Science Technical Report, 2003.

[25] Shammaa, M. H., Suzuki, H., and Ohtake, Y. Extraction of isosurfaces from multi-material ct volumetric data of mechanical parts. In *SPM '08: Proceedings of the 2008 ACM symposium on Solid and physical modeling* (New York, NY, USA, 2008), ACM, pp. 213–220.

[26] Stalling, D., Zckler, M., and Hege, H. C. Interactive segmentation of 3d medical images with subvoxel accuracy. In *Proc. CAR98 Computer Assisted Radiology and Surgery* (1998), pp. 137–142.

[27] Tiede, U., Schiemann, T., and Höhne, K. H. High quality rendering of attributed volume data. In *VIS '98: Proceedings of the conference on Visualization '98* (Los Alamitos, CA, USA, 1998), IEEE Computer Society Press, pp. 255–262.

[28] Wilson, O., VanGelder, A., and Wilhelms, J. Direct volume rendering via 3d textures. Tech. rep., Santa Cruz, CA, USA, 1994.

[29] Yuan, X., Zhang, N., Nguyen, M. X., and Chen, B. Volume cutout. *The Visual Computer (Special Issue of Pacific Graphics 2005) 21*, 8–10 (2005), 745–754.